

**Original citation:**

Tzimas, Angelos S., Dimopoulos, Athanasios I. and Karavasilis, Theodore L.. (2015) EC8-based seismic design and assessment of self-centering post-tensioned steel frames with viscous dampers. *Journal of Constructional Steel Research*, Volume 105 . pp. 60-73.

**Permanent WRAP url:**

<http://wrap.warwick.ac.uk/68972>

**Copyright and reuse:**

The Warwick Research Archive Portal (WRAP) makes this work of researchers of the University of Warwick available open access under the following conditions. Copyright © and all moral rights to the version of the paper presented here belong to the individual author(s) and/or other copyright owners. To the extent reasonable and practicable the material made available in WRAP has been checked for eligibility before being made available.

Copies of full items can be used for personal research or study, educational, or not-for-profit purposes without prior permission or charge. Provided that the authors, title and full bibliographic details are credited, a hyperlink and/or URL is given for the original metadata page and the content is not changed in any way.

**Publisher statement:**

© 2015 Elsevier, Licensed under the Creative Commons Attribution-NonCommercial-NoDerivatives 4.0 International <http://creativecommons.org/licenses/by-nc-nd/4.0/>  
<http://dx.doi.org/10.1016/j.jcsr.2014.10.022>

**A note on versions:**

The version presented here may differ from the published version or, version of record, if you wish to cite this item you are advised to consult the publisher's version. Please see the 'permanent WRAP url' above for details on accessing the published version and note that access may require a subscription.

For more information, please contact the WRAP Team at: [publications@warwick.ac.uk](mailto:publications@warwick.ac.uk)

warwick**publications**wrap  
  
highlight your research

<http://wrap.warwick.ac.uk/>

# **EC8-based seismic design and assessment of self-centering post-tensioned steel frames with viscous dampers**

Angelos S. Tzimas, Athanasios I. Dimopoulos, Theodore L. Karavasilis\*

*School of Engineering, University of Warwick, CV4 7AL Coventry, United Kingdom*

## **ABSTRACT**

This paper focuses on seismic design and assessment of steel self-centering moment-resisting frames (SC-MRFs) with viscous dampers within the framework of Eurocode 8 (EC8). Performance levels are defined with respect to drifts, residual drifts and limit states in the post-tensioned (PT) connections. A preliminary pushover analysis is conducted at the early phase of the design process to estimate rotations and axial forces in post-tensioned (PT) connections instead of using approximate formulae. Different designs of an SC-MRF with viscous dampers are considered to investigate all possible scenarios, i.e. use of dampers to achieve drifts significantly lower than the EC8 drift limit; to significantly reduce steel weight without exceeding the EC8 drift limit; or to reduce steel weight and achieve drifts lower than the EC8 drift limit. Nonlinear dynamic analyses using models capable of simulating all structural limit states up to collapse confirm the minimal-damage performance of the SC-MRFs. It is shown that the use of the preliminary pushover analysis makes the design procedure very accurate in predicting structural and non-structural limit states. Supplemental damping along with strict design criteria for the post-tensioned connections are found to significantly improve the seismic performance of the SC-MRFs. Moreover, the paper shows that SC-MRFs with viscous dampers have superior collapse resistance compared to conventional steel MRFs even when the SC-MRF is significantly lighter than the conventional MRF.

**KEY WORDS:** Self-centering; Post-tensioned; Seismic resilience; Collapse; Steel frames; Eurocode 8

\*Corresponding Author. Tel.: +44 (0)2476522363. *E-mail address:* T.Karavasilis@warwick.ac.uk

## 1. Introduction

Previous studies on seismic design and evaluation of conventional seismic-resistant systems, such as steel moment-resisting frames (MRFs) [1-3], showed that these systems experience significant inelastic deformations in structural members under the design basis earthquake (DBE; 475 yrs return period) [4]. Inelastic deformations result in structural damage and residual drifts, and therefore, in economic losses such as repair costs and downtime. Moreover, earthquake reconnaissance reports reveal large economic losses related to non-structural damage, e.g. failure of walls due to large storey drifts [5]. These losses highlight the need for resilient structures with the inherent potential to minimize structural and non-structural damage. Such structures should remain intact under the frequently occurred earthquake (FOE; return period of 95 years) and return to service within an acceptable short, if not immediate, time after the DBE. A resilient structure should also provide a low probability of collapse under the maximum considered earthquake (MCE; return period of 2500 yrs). The ATC-63 project sets a limit on the permissible probability of collapse under the MCE equal to 10% [6]. As this limit has been primarily set for conventional structural systems, lower probabilities of collapse should be offered by resilient structures.

Steel self-centering moment-resisting frames (SC-MRFs) using post-tensioned (PT) beam-column connections are a promising class of resilient structures. SC-MRFs exhibit softening force-drift behaviour and eliminate beam inelastic deformations and residual drifts as the result of gap opening developed in beam-column interfaces and elastic PT bars which clamp beams to the columns and provide self-centering capability. PT connections use yielding-based [7-13] or friction-based [14-17] energy dissipation devices, which are activated when gaps open and can be easily replaced if damaged. Seismic design procedures for SC-MRFs have been proposed in [18-19].

Steel MRFs equipped with passive dampers is another class of resilient structures. Previous analytical and experimental research showed that steel MRFs with elastomeric dampers can be designed to be lighter and perform better than conventional steel MRFs under the DBE [20-21]. However, it was shown that it is generally not feasible to design steel MRFs with passive dampers at a practical size to eliminate inelastic deformations in main structural members under the DBE [20-21]. To address this issue, a seismic design strategy for steel MRFs, which isolates damage in removable steel energy dissipation devices and uses in parallel viscous dampers to reduce drifts, has been proposed [22]. A study shows that supplemental viscous damping does not always ensure adequate reduction of residual drifts [23]. A recent work evaluates the seismic collapse resistance of steel MRFs with viscous dampers and shows that supplemental viscous damping does not always guarantee a better seismic collapse resistance when the strength of the steel MRF with dampers is lower or equal to 75% of the strength of a conventional steel MRF [24].

The use of viscous dampers in parallel to self-centering precast concrete base rocking walls has been proposed as an effective way to control peak story drifts and residual drifts [25]. The parallel combination of hysteretic and viscous energy dissipation along with a friction slip mechanism in series connected to the viscous energy dissipation mechanism were found to achieve high levels of seismic performance for self-centering systems [26]. A displacement-based seismic design procedure for self-centering frames using combinations of energy dissipation mechanisms has been proposed and evaluated in [27].

Research towards the standardization of steel SC-MRFs within the framework of Eurocode 8 (EC8) is missing, while their collapse resistance for seismic intensities higher than the MCE has not been thoroughly studied. Moreover, the effectiveness of the seismic design strategy that combines steel SC-MRFs with viscous dampers to simultaneously control peak story drifts and residual story drifts has not been assessed.

This paper focuses on seismic design and assessment of steel SC-MRFs with viscous dampers within the framework of EC8. SC-MRFs are using the recently developed PT connection with web hourglass shape pins (WHPs) [11-12]. Performance levels are defined with respect to drifts, residual drifts and limit states in the PT connections. A preliminary pushover analysis is conducted at the early phase of the design process to estimate rotations and axial forces in PT connections instead of using approximate formulae. A prototype building is designed as a SC-MRF with or without viscous dampers. Different designs of the SC-MRF with viscous dampers are considered to investigate all possible scenarios, i.e. use of dampers to achieve drifts significantly lower than the EC8 drift limit; to significantly reduce steel weight without exceeding the EC8 drift limit; or to reduce steel weight and achieve drifts lower than the EC8 drift limit. Nonlinear dynamic analyses in OpenSees [28] using models capable of simulating all structural limit states up to collapse confirm the minimal-damage performance of the SC-MRFs, their superior collapse resistance, and the accuracy of the seismic design procedure.

## 2. SC-MRF using PT connections with WHPs

### 2.1 Structural details

Fig. 1(a) shows a SC-MRF using PT connections with WHPs and Fig. 1(b) shows an exterior PT connection with WHPs [11-12]. Two high strength steel bars located at the mid depth of the beam, one at each side of the beam web, pass through holes drilled on the column flanges. The bars are post-tensioned and anchored to the exterior columns. WHPs are inserted in aligned holes on the beam web and on supporting plates welded to the column flanges. Energy is dissipated through inelastic bending of the WHPs that have an optimized hourglass shape (Fig. 1(c)) with enhanced fracture capacity [29]. The beam web and the beam flanges are reinforced with steel plates. The panel zone is strengthened with doubler and continuity plates. A fin plate welded on the column flange and bolted on the beam web is used for easy erection and resistance against gravity loads before post-tensioning. Slotted holes on the beam web ensure negligible influence of the fin plate on the PT connection behaviour. To avoid brittle failures in the PT connection due to beam web or flange inelastic buckling (seen in experiments and finite element analyses [11-12]), the use of a fuse-PT bar mechanism is adopted, i.e. similar in concept to what has been used in [30]. As shown in Fig. 1(b), a short stocky steel beam (referred to as 'fuse') is welded on a strong plate bolted on the exterior column flange to enable replacement. PT bars are anchored on a stiff plate welded on the exterior face of the fuse. The fuse is designed to yield at a predefined force level to limit the peak force and elongation of the PT bars.

A discontinuous steel-concrete composite slab (details shown in Fig. 2) is used to avoid damage in the slab as the gaps in the PT connections open and close (see Fig. 3(b)), i.e. similar to the solutions proposed in [10, 19]. Shear studs for composite action are welded only on the secondary beams. The slab discontinuity is achieved by using two angle sections sliding on the beam framing perpendicularly to the SC-MRF columns. The slab reinforcing mesh is discontinued at the level of the angles. The secondary beams and the slab are placed after post-tensioning. The slab diaphragm eliminates beam shortening, and so, the internal axial forces in the beams remain constant and equal to those due to initial post-tensioning of the PT bars. Any further increase in the PT bars forces due to elongation under gap opening is transferred to the beam-column interfaces by the slab diaphragm.

### 2.2 PT connection behaviour

Fig. 3(a) shows the free body diagram of an external PT connection where  $d_{1u}$  and  $d_{1l}$  are the distances of the upper and lower WHPs from the center of rotation that is assumed to be at the inner edge of the beam flange reinforcing plates;  $d_2$  is the distance of the PT bars from the center of rotation;  $T$  is the total force in both PT bars;  $F_{WHP,u}$  and  $F_{WHP,l}$  are the forces in the upper and lower WHPs;  $C_F$  is the compressive force in the beam-column interface;  $V_{C1u}$  and  $V_{C1l}$  are the shear forces in the upper and lower column,  $M$  is the PT connection moment,  $V$  is the beam shear force; and  $N$  is the horizontal clamping force that is transferred to the beam-column interface through the slab diaphragm and the beam. Fig. 3(b) shows the SC-MRF expansion due to rotations  $\theta$  in the PT connections.  $N$  is given by

$$N = T + V_{C1u} - V_{C1l} \quad (1.a)$$

for the external connection of Fig. 3(a) and by

$$N = T + \sum (V_{Ciu} - V_{Cil}) + \sum F_{Dj} \quad (1.b)$$

for an internal connection of Fig. 3(b) where  $V_{Ciu}$  and  $V_{Cil}$  are the shear forces developed in all the columns  $i$  and  $F_{Dj}$  are the slab inertia forces transferred (by the secondary beams) to the mid-depth of all the beams  $j$  up to the point of the examined internal connection. Eqs (1.a) and (1.b) are derived by horizontal equilibrium of the free body diagrams of Figs 3(a) and 3(b).

Fig. 4(a) shows the theoretical cyclic  $M$ - $\theta$  behaviour of the PT connection with WHPs.  $M$  is given by

$$M = M_N + M_{WHP} \quad (2)$$

where  $M_N$  is the moment contribution from  $N$  (shown in Fig. 4(b)) and  $M_{WHP}$  is the moment contribution from the WHPs (shown in Fig. 4(c)). Similar expressions can be found in the literature [11, 18, 19]. After decompression of the PT connection (Point 1 in Fig. 4(a)), gap opens and the behaviour becomes nonlinear elastic with rotational stiffness  $S_1$ . At point 2, the upper WHPs yield and  $M$  continues to increase with slope  $S_2$ . At point 3, the lower WHPs yield and  $M$  continues to increase with slope  $S_3$ . At point 4, the fuse yields and  $M$  continues to increase with slope  $S_4$ . When loading is reversed, the connection begins to unload until the gap closes. Equations to calculate  $S_{WHP,1}$  to  $S_{WHP,3}$ ,  $S_{N,1}$  to  $S_{N,2}$ ,  $S_1$  to  $S_4$  and  $\theta_2$  to  $\theta_4$  are provided in Section 2.3.

The  $M_{WHP}$ - $\theta$  behaviour is multi-linear elastoplastic. When loading is reversed and until the gap closes, the fuse unloads with its initial stiffness (without yielding in the opposite direction) and the PT bars with their elastic stiffness. This explains why the  $M_N$ - $\theta$  curve fully unloads with its initial stiffness. Due to the residual plastic shortening of the fuse, the force in the PT bars when the gap closes is lower than their initial post-tensioning force.

### 2.3 Design procedure for the PT connection

Given the rotations of the PT connection under the DBE and MCE (i.e.  $\theta_{DBE}$  and  $\theta_{MCE}$ ) and the corresponding forces  $V_{Ciu}$ ,  $V_{Cil}$  and  $F_{Dj}$  from a preliminary pushover analysis of the SC-MRF that is discussed in Section 3, the design procedure involves sizing of the connection components (e.g. PT bars, WHPs, fuse, reinforcing plates) to achieve a target connection performance, and has the following steps:

*Step (1): Calculate the initial post-tensioning force.* Select a value for the ratio  $M_{IGO}/M_{pl,b}$  where  $M_{IGO}$  is the moment at point 2 in Fig. 4(a) and  $M_{pl,b}$  is the plastic moment of resistance of the beam.  $M_{IGO}/M_{pl,b}$  should be less than one for the SC-MRF to have base shear strength comparable to that of conventional MRFs. Select a value for the ratio  $M_d/M_{IGO}$  where  $M_d$  is the moment contribution from the total initial post-tensioning force  $T_0$  in both PT bars. In past research,  $M_d$  is referred as decompression moment [18, 19].  $M_d/M_{IGO}$  should be larger than

0.5 to approximately achieve self-centering behaviour of the PT connection [14, 18] (the effectiveness of the selected  $M_d/M_{IGO}$  value is accurately evaluated in design Step 4).  $T_0$  is given by

$$T_0 = \frac{M_d}{d_2} \quad (3)$$

*Step (2): Design the PT bars and the fuse device.* Assume an initial PT bar diameter  $d_{PT}$  and calculate the total yield force of both PT bars,  $T_y$ , by

$$T_y = 0.5 \cdot f_{y,PT} \cdot \pi \cdot d_{PT}^2 \quad (4)$$

where  $f_{y,PT}$  is the yield strength of the PT bar material. Select the rotation  $\theta_4$  (Fig. 4(a)) where the fuse yields (see examples in Section 4) and calculate  $T$  by

$$T(\theta) = T_0 + d_2 \cdot \theta \cdot K_{PT} \quad \text{for} \quad \theta < \theta_4 \quad (5.a)$$

$$T(\theta) = T_0 + d_2 \cdot \theta_4 \cdot K_{PT} + d_2 \cdot (\theta - \theta_4) \cdot \frac{K_{PT} \cdot K_{fuse}}{K_{PT} + K_{fuse}} \quad \text{for} \quad \theta \geq \theta_4 \quad (5.b)$$

where  $K_{PT}$  is the total axial stiffness of both PT bars and  $K_{fuse}$  is the post-yielding axial stiffness of the fuse associated with the specific connection to be designed. Eq. (5.a) ignores the high initial elastic stiffness of the fuse which should be significantly higher than  $K_{PT}$ .  $K_{PT}$  and  $K_{fuse}$  are calculated by

$$K_{PT} = \frac{E_{PT} \cdot A_{PT} \cdot \sum_{i=1}^n \Delta_{gap,i}}{L_{PT} \cdot \Delta_{gap}} \quad (6)$$

$$K_{fuse} = \alpha_H \cdot \frac{E_{fuse} \cdot A_{fuse} \cdot \sum_{i=1}^n \Delta_{gap,i}}{L_{fuse} \cdot \Delta_{gap}} \quad (7)$$

where  $E_{PT}$  and  $E_{fuse}$  are the Young's moduli,  $A_{PT}$  and  $A_{fuse}$  are the total cross-section areas, and  $L_{PT}$  and  $L_{fuse}$  are the total lengths of the PT bars and the fuse, respectively.  $\alpha_H$  is the hardening ratio of the fuse material.  $\Delta_{gap,i}$  is the gap opening at the mid-depth of the beam of a connection  $i$ ,  $n$  is the total number of connections per floor, and  $\Delta_{gap}$  is the gap opening of the specific connection to be designed. The gap opening of any connection can be calculated as

$$\Delta_{gap,i} = d_{2,i} \cdot \theta_1 \quad (8)$$

$A_{fuse}$  is calculated by

$$A_{fuse} = T(\theta_4) / f_{y,fuse} \quad (9)$$

where  $f_{y,fuse}$  is the yield strength of the fuse material. Select the safety factor against PT bar yielding  $\gamma_{PT}$  (recommendations are given in Section 4) and check if  $T_y/T(\gamma_{PT} \cdot \theta_{MCE}) \geq 1.0$ . If  $T_y/T(\gamma_{PT} \cdot \theta_{MCE}) < 1.0$ , design Step 2 should be repeated with a larger  $d_{PT}$ .

The main difference of Eqs (5.a) and (5.b) with those proposed in [18, 19] is the inclusion of the effect of the fuse device in the calculation of the PT bar force. In addition, Eqs (5.a) and (5.b) do not consider beam shortening as this is eliminated by the slab diaphragm (see previous discussion in Section 2.1).

*Step (3): Design the WHPs.* Select the number of upper and lower WHPs,  $n_{WHPs}$  ( $=2$  in Fig. 1), and calculate the required yield force of one WHP,  $F_{WHP,y}$ , from

$$F_{WHP,y} = \frac{d_{1u}}{n_{WHPs}} \cdot \frac{M_{IGO} - M_N(\theta_2)}{d_{1u}^2 + d_{1l}^2} \quad (10)$$

by substituting  $M_d$  for  $M_N(\theta_2)$  as  $M_N(\theta_2)$  is still unknown. The required plastic moment of resistance of the WHPs cross-section,  $M_{pl,WHP}$ , is calculated by

$$M_{pl,WHP} = 0.25 \cdot F_{WHP,y} \cdot L_{WHP} \quad (11)$$

where  $L_{\text{WHP}}$  is the length of half a WHP (Fig. 1(c)). The external,  $D_e$ , and internal,  $D_i$ , diameters of the WHP (Fig. 1(c)) are designed by using

$$D_e = \left( \frac{6 \cdot M_{\text{pl,WHP}}}{f_{y,\text{WHP}}} \right)^{\frac{1}{3}} \quad (12)$$

$$D_i \geq \sqrt{\frac{2 \cdot F_{y,\text{WHP}} \cdot \sqrt{3}}{\pi \cdot f_{y,\text{WHP}}}} \quad (13)$$

where  $f_{y,\text{WHP}}$  is the yield strength of the WHP material. The elastic stiffness of a WHP is calculated from [11-12]

$$K_{\text{fe}} = \frac{18 \cdot \pi \cdot D_e^3 \cdot D_i \cdot E_{\text{WHP}} \cdot G_{\text{WHP}}}{40 \cdot E_{\text{WHP}} \cdot D_e^2 \cdot L_{\text{WHP},i} + 48 \cdot G_{\text{WHP}} \cdot L_{\text{WHP},i}^3} \quad (14)$$

where  $E_{\text{WHP}}$  is the Young's modulus and  $G_{\text{WHP}}$  the shear modulus of the WHP material.  $\theta_2$  and  $\theta_3$  (Fig. 4(c)) are calculated by

$$\theta_2 = F_{\text{WHP},y} / (K_{\text{fe}} \cdot d_{1u}) \quad (15)$$

$$\theta_3 = F_{\text{WHP},y} / (K_{\text{fe}} \cdot d_{1l}) \quad (16)$$

With  $\theta_2$  known,  $M_{\text{N}}(\theta_2)$  is calculated by

$$M_{\text{N}}(\theta_2) = M_d + K_{\text{PT}} \cdot d_2^2 \cdot \theta_2 + S_{\text{F}} \cdot \theta_2 \quad (17)$$

where  $S_{\text{F}}$  is the additional rotational stiffness of the frame due to the columns restraint that opposes gap opening.  $S_{\text{F}}$  is calculated by

$$S_{\text{F}} = \frac{N(\theta_2) - T(\theta_2)}{\theta_2} \cdot d_2 \quad (18)$$

where  $(N(\theta_2) - T(\theta_2))$  is calculated from Eq. (1) by using values for  $V_{\text{Cil}}$ ,  $V_{\text{Ciu}}$  and  $F_{\text{Dj}}$  from a preliminary pushover analysis (discussed in Section 3). The new value of  $M_{\text{N}}(\theta_2)$  is used in Eq. (10) and the WHP design process (Eqs (10)-(18)) is repeated.

*(Step 4): Self-centering capability.* To check whether the PT connection provides self-centering behaviour up to a desired rotation  $\theta_{\text{SC}}$ , the following relations should be satisfied:

$$M_d \geq \theta_2 \cdot (S_1 - S_2) + \theta_3 \cdot (S_2 - S_3) \quad \text{for } \theta_{\text{SC}} < \theta_4 \quad (19.a)$$

$$M_d \geq \theta_2 \cdot (S_1 - S_2) + \theta_3 \cdot (S_2 - S_3) + (\theta_{\text{SC}} - \theta_4) \cdot (S_3 - S_4) \quad \text{for } \theta_{\text{SC}} \geq \theta_4 \quad (19.b)$$

where  $S_1$  to  $S_4$  (Fig. 4(a)) are given by

$$S_1 = S_{\text{N},1} + S_{\text{WHP},1} + S_{\text{F}}(\theta) \approx K_{\text{PT}} \cdot d_2^2 + 2 \cdot K_{\text{fe}} \cdot (d_{1l}^2 + d_{1u}^2) \quad (20.a)$$

$$S_2 = S_{\text{N},1} + S_{\text{WHP},2} + S_{\text{F}}(\theta) \approx K_{\text{PT}} \cdot d_2^2 + 2 \cdot (K_{\text{fe}} \cdot d_{1l}^2 + K_{\text{fp}} \cdot d_{1u}^2) \quad (20.b)$$

$$S_3 = S_{\text{N},1} + S_{\text{WHP},3} + S_{\text{F}}(\theta) \approx K_{\text{PT}} \cdot d_2^2 + 2 \cdot K_{\text{fp}} \cdot (d_{1l}^2 + d_{1u}^2) \quad (20.c)$$

$$S_4 = S_{\text{N},2} + S_{\text{WHP},3} + S_{\text{F}}(\theta) \approx \frac{K_{\text{PT}} \cdot K_{\text{fuse}}}{K_{\text{PT}} + K_{\text{fuse}}} \cdot d_2^2 + 2 \cdot K_{\text{fp}} \cdot (d_{1l}^2 + d_{1u}^2) \quad (20.d)$$

and  $K_{\text{fp}}$  is the post-yield stiffness of a WHP that is assumed equal to 2% the initial stiffness. If Eq. (19) is not satisfied, return to design Step 1 and repeat the design procedure with a higher  $M_d/M_{\text{IGO}}$  ratio. Eqs (19.a) and (19.b) were derived by following the procedure described in [8] but include also the effect of the fuse on the self-centering capability of the PT connection.

*(Step 5): Design the reinforcing plates.* Following the design procedure in [18], the length,  $L_{\text{tp}}$ , and the area,  $A_{\text{tp}}$ , of the beam flange reinforcing plate (Fig. 1(b)) are designed to control beam flange yielding at  $\theta = \theta_{\text{DBE}}$ .  $L_{\text{tp}}$  is given by

$$L_{rp} \geq \frac{L_b}{2} \cdot \frac{M - M_{rp}}{M} \quad (21)$$

where  $L_b$  is the beam clear length and  $M_{rp}$  is the moment at the end of the reinforcing plate.  $M_{rp}$  is calculated as a function of the beam internal axial force and a predefined target value of  $\varepsilon_c/\varepsilon_y$  where  $\varepsilon_c$  the maximum compressive strain in the beam flange at the end of the reinforcing plate and  $\varepsilon_y$  the yield strain of the beam material [18]. As was discussed, the beam internal axial force remains constant due to the slab diaphragm and can be conservatively assumed equal to  $T_0$  without considering the column restraint.  $M$  depends on the rotation  $\theta$ , i.e. for  $\theta_2 < \theta < \theta_3$

$$M = d_{1u} \cdot n_{WHPs} \cdot [F_{WHP,y} + K_{fp} \cdot d_{1u} \cdot (\theta - \theta_2)] + d_{1l}^2 \cdot n_{WHPs} \cdot K_{fe} \cdot \theta + d_2 \cdot N(\theta) \quad (22.a)$$

and for  $\theta \geq \theta_3$

$$M = n_{WHPs} \cdot F_{WHP,y} \cdot d_{1u} + n_{WHPs} \cdot F_{WHP,y} \cdot d_{1l} + n_{WHPs} \cdot [d_{1u}^2 \cdot K_{fp} \cdot (\theta - \theta_2) + d_{1l}^2 \cdot K_{fp} \cdot (\theta - \theta_3)] + d_2 \cdot N(\theta) \quad (22.b)$$

The minimum  $A_{rp}$  to avoid beam flange yielding at the beam-column interface is calculated by

$$A_{rp} = \frac{C_F - b_f \cdot t_f \cdot f_{y,b}}{f_{y,rp}} \quad (23)$$

where  $f_{y,rp}$  is the yield strength of the reinforcing plate material and  $t_f$  and  $b_f$  are the thickness and width of the beam flange, respectively. For  $\theta_2 < \theta < \theta_3$ ,  $C_F$  (Fig. 3(a)) is obtained by

$$C_F = N(\theta) + n_{WHPs} \cdot [F_{WHP,y} + d_{1u} \cdot K_{fp} \cdot (\theta - \theta_2) + d_{1l} \cdot K_{fe} \cdot \theta] \quad (24.a)$$

and for  $\theta > \theta_3$  by

$$C_F = N(\theta) + 2 \cdot n_{WHPs} \cdot F_{WHP,y} + n_{WHPs} \cdot [d_{1u} \cdot K_{fp} \cdot (\theta - \theta_2) + d_{1l} \cdot K_{fp} \cdot (\theta - \theta_3)] \quad (24.b)$$

Eqs (21) – (24.b) were derived following the design methodology described in [18]. The beam web reinforcing plates and the supporting plates are designed to avoid yielding under the peak WHP bearing forces following the design procedure in [29]. The panel zones are designed according to EC8 [4] and EC3 [31] and are reinforced with doubler and continuity plates.

### 3. Performance-based seismic design procedure

The seismic design procedure within the framework of EC8 for steel SC-MRFs with or without viscous dampers ensures a pre-defined structural and non-structural target building performance, and has the following steps:

*(Step 1): Define target building performance.* Structural limit states include limit states of the PT connections, yielding and plastic hinge formation at the column bases, and limit values for the maximum residual storey drift,  $\theta_{s,res}$ . Limit states of the PT connections include WHPs yielding (controlled by  $M_{IGO}/M_{pl,b}$ ), fuse activation (controlled by  $\theta_4$ ), PT bar yielding (controlled by  $\gamma_{PT}$ ), beam flange yielding at the end of the reinforcing plate (controlled by  $\varepsilon_c/\varepsilon_y$ ), beam flange yielding at the beam-column interface (controlled by Eq. (23)), and self-centering behaviour (controlled by  $M_d/M_{IGO}$  and Eq. (19)). Non-structural limit states include limit values for the peak storey drift,  $\theta_{s,max}$ . For example, the following target building performance can be defined for a SC-MRF with viscous dampers and PT connections with WHPs by associating limit states with seismic intensities: *Operational* under the FOE: no yielding in beams and column bases;  $\theta_{s,max}$  lower than the 'damage limitation' values of EC8; and PT connection decompression and modest yielding in WHPs. *Rapid Return to Occupancy* under the DBE: elimination of  $\theta_{s,res}$ ; modest or no yielding in the beam flanges; modest or no yielding in base columns; low  $\theta_{s,max}$  to ensure rapid repair of damaged drift-



sensitive non-structural elements; and yielding and rapid replacement of WHPs. *Life Safety and Reparability* under the MCE: no beam plastic hinge formation; modest base column plastic hinge rotations; and  $\theta_{s,res}$  lower than the global sway imperfections defined in EC3 [31].

(Step 2): *Select supplemental damping*. The supplemental damping ratio  $\xi_s$  is added to the inherent damping ratio to provide a total damping ratio  $\xi_t$  which is then used to calculate the damping reduction factor  $B$  [32] (or  $\eta$  in EC8 [4]). This factor is used to scale down the elastic design spectrum of EC8.

(Step 3): *Design beams and columns*. The beam and column cross-sections are sized by designing the building as a conventional steel MRF on the basis of the modal response spectrum analysis of EC8 and with respect to the highly damped spectrum of Step 2. A strength-based design for the DBE is first performed by reducing the highly damped spectrum with the behaviour factor  $q$  (i.e., 6.5 in EC8 for high ductility class MRFs).  $\theta_{s,max}$  is then estimated on the basis of the equal displacement rule of EC8 to check the design against the FOE and DBE  $\theta_{s,max}$  criteria of Step 1. The DBE ultimate limit state of EC8 is satisfied by enforcing the capacity design rule and the local ductility details for steel MRFs, and by taking into account second-order effects (P- $\Delta$ ) through the storey drift sensitivity coefficient [4].

(Step 4): *Design fluid viscous dampers*. Given  $\xi_s$  from Step 2 and the fundamental period of vibration  $T$  from Step 3, nonlinear viscous dampers are designed by using the formula [32]:

$$\xi_s = \frac{\sum_j (2\pi)^a T^{2-a} \lambda_j f_j^{1+a} c_j u_r^{a-1} (\phi_j - \phi_{j-1})^{1+a}}{8\pi^3 \sum_j m_j \varphi_j^2} \quad (25)$$

where  $j$  denotes a specific storey,  $\alpha$  is the velocity exponent of the nonlinear viscous dampers,  $\lambda_j$  a dimensionless parameter that depends on  $\alpha$ ,  $f_j$  the cosine of the angle of the damper centerline to the horizontal (e.g.  $f_j=1.0$  for horizontal damper placement),  $c_j$  the damper constant,  $u_r$  the amplitude of the roof displacement,  $m_j$  the storey mass, and  $\varphi_j$  the modal coordinate of the first mode shape. Eq. (25) assumes that viscous dampers are supported by braces stiff enough so that drift produces damper rather than brace deformation. Dampers and supporting braces can be inserted in a gravity frame of the building as shown in Fig. 5. Eq. (25) suggests that the required  $\xi_s$  can be provided by different combinations of  $c_j$ . A recent work showed small differences in the seismic performance of steel MRFs with viscous dampers designed for the same  $\xi_s$  yet different methods (two advanced based on numerical optimization and three simplified) of distributing  $c_j$  along the height of the building [33]. Based on the latter finding and on recent research results presented in [24], viscous dampers can be sized to satisfy a simple stiffness proportional distribution, i.e.  $c_j = \varepsilon K_j$ , where  $K_j$  is the horizontal storey stiffness of the SC-MRF and  $\varepsilon$  is a constant that is obtained by substituting  $c_j = \varepsilon K_j$  into Eq. (25). The columns and braces of the gravity frame with dampers are designed to avoid buckling under the peak damper forces which are estimated using simplified procedures in [32]. In case of large not practical  $c_j$  values, Steps 2 to 4 should be repeated by selecting a lower  $\xi_s$  value in Step 2.

(Step 5): *Preliminary pushover analysis*. A preliminary pushover analysis is performed using a simple model with nonlinear beam-column elements for the columns, elastic elements for the beams and nonlinear rotational springs at the ends of the beams to simulate the M- $\theta$  behaviour of the PT connections. The rotational springs should have a large initial stiffness (e.g. 60 times the beam flexural stiffness to provide stable and accurate results), a yield moment equal to  $M_{IGO}$  calculated from an appropriate  $M_{IGO}/M_{pl,b}$  value as explained in Section 2.3, and post-yield stiffness equal to  $K_{PT} \cdot d_2^2$  where  $K_{PT}$  is estimated from Eq. (6).  $A_{PT}$  in Eq. (6) is calculated on the basis of an appropriate  $M_d/M_{IGO}$  value as explained in Section

2.3. The required PT bar diameter can be estimated by assuming  $T_0/T_y \approx 0.5$ , which approximately ensures that PT bars avoid yielding under large rotations in the PT connections [14]. At each step of the pushover analysis, the connection rotations and member forces are post-processed. PT connection rotations and member forces of a SC-MRF can be also estimated using approximate formulae, such as those presented in [18], instead of using pushover analysis. However, pushover analysis is now available in most commercial software packages and is also promoted by EC8 as an alternative to linear analysis methods. In addition, the limit states of Step 1 associated with base column yielding and plastic hinge formation are checked. Modest yielding at column bases, i.e. low rotation ductility values (e.g. less than 2 [34]), under the DBE and MCE along with full self-centering capability of the PT connections will ensure satisfaction of the  $\theta_{s,res}$  criteria of Step 1.

(Step 6): *Design PT connections.* Given the results of the preliminary pushover analysis of Step 5, PT connections are designed using the procedure in Section 2.3 to achieve the target connection performance defined in Step 1.

## 4. SC-MRFs with viscous dampers

### 4.1 Prototype building

Fig. 5(a) shows the plan view of a 5-storey, 5-bay by 3-bay prototype building having two identical SC-MRFs in the 'x' plan direction. Viscous dampers are inserted in the interior gravity frames (with pinned beam-column and column base connections) that are coupled with the perimeter SC-MRFs through the floor diaphragm to form SC-MRFs with viscous dampers as shown in Fig. 5(b). This paper focuses on one of the SC-MRFs with dampers. The building has ductile non-structural elements, and so,  $\theta_{s,max}$  should be lower than 0.75% under the FOE according to EC8. The DBE is expressed by the Type 1 elastic response spectrum of EC8 with peak ground acceleration equal to 0.35g and ground type B. The FOE has intensity of 40% (reduction factor  $\nu=0.4$  in EC8) the intensity of the DBE. The MCE has intensity of 150% the intensity of the DBE. The model used for the design is based on the centerline dimensions of the SC-MRF without accounting for the finite panel zone dimensions. A 'lean-on' column is included in the model to account for the P- $\Delta$  effects of the vertical loads acting on the gravity columns in the tributary plan area (half of the total plan area) assigned to the SC-MRF. A rigid diaphragm constraint is imposed at the nodes of each floor level for the design. The steel yield strength is equal to 355 MPa for the columns, 275 MPa for the beams, 835 MPa for PT bars, 235 MPa for the WHPs, 275 MPa for the beam reinforcing plates, and 235 MPa for the fuse. Nonlinear viscous dampers are designed with a horizontal configuration (i.e.  $f_j=1$ ) and  $a=0.5$ . The inherent damping ratio of the SC-MRF is equal to 3%.

### 4.2 Design cases

Different versions of the SC-MRF with viscous dampers (Fig. 5(b)) are designed to investigate different design scenarios. The PT connections are designed for  $M_{IGO}/M_{pl,b}=0.65$  and  $M_d/M_{IGO}=0.6$ . An  $\varepsilon_c/\varepsilon_y$  value equal to 2 under the DBE was used for conventional performance SC-MRFs, i.e. according to the recommendation in [18]. To achieve structural and non-structural damage harmonization, stricter design criteria ( $\varepsilon_c/\varepsilon_y$ ,  $\gamma_{PT}$  and  $\theta_4$ ) are used for the PT connections of the SC-MRFs designed for lower  $\theta_{s,max}$ . Table 1 provides a comparison of the steel weight,  $T$ ,  $\xi_t$  and design criteria of the SC-MRFs which are discussed below:

*CP3D100W*: Conventional performance SC-MRF without viscous dampers ( $\xi_t=3\%$ ).

*HP20D100W*: High performance SC-MRF with viscous dampers ( $\xi_t = 20\%$ ). It demonstrates the design scenario where viscous dampers are used to achieve  $\theta_{s,max}$  significantly lower than the EC8 limit. It also demonstrates the design scenario where strict design criteria for the PT connections along with a low  $\theta_{s,max}$  target value are enforced to genuinely achieve seismic resilience. Its target performance led to the same cross sections and PT connections details with those of CP3D100W.

*CP11D86W*: Conventional performance SC-MRF with viscous dampers ( $\xi_t = 11\%$ ). Its steel weight is 86% the steel weight of CP3D100W. It represents the design scenario where viscous dampers are used to reduce steel weight without exceeding the EC8  $\theta_{s,max}$  limit.

*HP19.5D86W*: High performance SC-MRF with viscous dampers ( $\xi_t = 19.5\%$ ). It represents the design scenario where viscous dampers are used to reduce steel weight and achieve  $\theta_{s,max}$  lower than the EC8 limit. Its target performance led to the same cross sections and PT connections details with those of CP11D86W.

*CP22D70W*: Conventional performance SC-MRF with viscous dampers ( $\xi_t = 22\%$ ). Its steel weight is 70% the steel weight of CP3D100W. It represents the design scenario where viscous dampers are used to significantly reduce steel weight without exceeding the EC8  $\theta_{s,max}$  limit.

Table 2 provides the  $\theta_{DBE}$  and  $\theta_{MCE}$  (from preliminary pushover analyses; Step 5 in Section 3) used to design the PT connections of the SC-MRFs. Tables 3-5 provide the beams and columns cross-sections,  $d_{PT}$  and  $T_0$ ,  $L_{TP}$  and  $A_{TP}$ ,  $A_{fuse}$ , and  $c$  of the SC-MRFs.

A conventional steel MRF without dampers has been also designed for comparison with the SC-MRFs. This MRF has the same cross-sections and the same drift performance with the CP3D100W SC-MRF.

## 5. Nonlinear models

Models for the SC-MRFs are developed in OpenSees as shown in Fig. 6 based on a recently proposed simplified model [13], which was calibrated against experimental results and found capable to accurately simulate the PT connection behaviour. The columns and the reinforced lengths of the beams are modelled as nonlinear force-based beam-column fiber elements. Fibers have bilinear elastoplastic stress-strain behaviour (Steel01 in OpenSees) with post-yield stiffness ratio of 0.003. The assumption of stable hysteresis for the columns is fully justified as heavy columns with webs and flanges of low slenderness (e.g. compact HEB sections in Tables 3-5) do not show cyclic deterioration even under large drifts [35]. Beam local buckling is expected just after the end of the reinforcing plates, and therefore, the unreinforced lengths of the beams are modelled as elastic elements with zero length rotational springs at their ends that exhibit strength and stiffness deterioration [36].

Rigid elastic beam-column elements are used to model the beam-column interface. To capture the gap opening mechanism in the beam-column interface, three zero-length contact spring elements are placed at equal spaces along the beam flange thickness. These contact springs have an elastic compression-no tension force-displacement behaviour (ENT material in OpenSees) with compression stiffness of 20 times the axial stiffness of the beam. Larger values for this stiffness were found to produce practically the same results but with more iterations to achieve convergence in nonlinear analysis. Two zero-length hysteretic springs are placed at the exact locations of WHPs along the depth of the beam web. These springs are associated with a smooth Giuffre-Menegotto-Pinto model with isotropic hardening (Steel 02 material in OpenSees) as recent experimental studies show that WHPs have stable hysteresis and do not fracture under collapse loading protocols associated with storey drifts of more than 10% [29].

Panel zones are modelled using the Scissors model [37] which introduces four additional rigid elastic beam-column elements and two nodes in the panel zone centre connected with two zero-length rotational springs. These springs have bilinear elastoplastic hysteresis (Steel01 material in OpenSees) with properties that reflect the contribution of the column web (including doubler plates) and the column flanges in the shear force - shear deformation panel zone behaviour.

Fuse elements are modelled as zero length axial translational springs attached to the exterior nodes of the panel zones of the left exterior column. These springs have a bilinear elastoplastic hysteresis with initial stiffness equal to  $E_{\text{fuse}} \cdot A_{\text{fuse}} / L_{\text{fuse}}$  and a 0.002 post-yield stiffness ratio.

PT bars are modelled as a truss element running parallel to the beam center-line axis and connected to the exterior node of the fuse element (left exterior column) and to the exterior node of the panel zones of the right exterior column. The truss element has a cross-section area equal to  $A_{\text{PT}}$  and material with bilinear elastoplastic hysteresis. To account for post-tensioning, an initial strain equal to  $T_0 / (A_{\text{PT}} \cdot E_{\text{PT}})$  is imposed to the truss element. Post-tensioning results in axial shortening of the beams and column deflections which decrease the post-tensioning force. To avoid this decrease, the initial strain in the truss element is increased to ensure that the post-tensioning force in the PT bars is equal to  $T_0$  after beam shortening.

To account for P- $\Delta$  effects, the gravity columns associated with one of the two lateral resisting frames of the plan in Fig. 5(a) are modelled as 3 lean-on columns, i.e. one for each bay of the frame. Diaphragm action is modelled with truss elements connecting the lean on columns nodes to nodes defined along the length of the beams at the points where secondary beams are placed. These trusses have stiffness of 100 times the axial beam stiffness.

Nonlinear viscous dampers are modelled with zero length elements (Viscous material of OpenSees), while their supporting braces are modelled with elastic braces as they are strong enough to avoid buckling. In the analytical model, the damper limit states caused by their stroke limit are not considered, i.e. it is assumed that dampers will be manufactured with enough stroke to avoid reaching their limit states even under very large storey drifts.

The connections of the conventional MRF are assumed to be rigid and have full strength, while beams are modeled as elastic elements with zero length rotational springs at their ends that exhibit strength and stiffness deterioration [36]. Columns and panel zones are modeled as described above for the SC-MRFs.

The OpenSees models for the SC-MRFs and the conventional MRF include the effect of the panel zone stiffness, and so, result in shorter  $T$  values than those shown in Table 1 that are based on the centerline models used for design.  $T$  from the OpenSees models is 1.00 s. for the CP3D100W and the HP20D100W, 1.35 s. for the CP11D86W and the HP19.5D86W, 1.95 s. for the CP22D70W, and 1.18 s. for the conventional MRF.

## 6. Monotonic and cyclic base shear vs roof drift behaviour

Fig. 7 shows the base shear coefficient ( $V/W$ ;  $V$ :base shear and  $W$ :seismic weight) - roof drift ( $\theta_r$ ) behaviour of the SC-MRFs and the conventional MRF from nonlinear monotonic static (pushover) analysis under an inverted triangular force distribution, similar to that specified in EC8 [4]. A nonlinear force-controlled static analysis under gravity loads and the applied post-tensioning is first performed. The stiff truss elements that simulate diaphragm action are not included in the SC-MRF models for this analysis to allow post tensioning and initial beam shortening without the slab presence. Then, the stiff truss elements are added into the model and a displacement-controlled pushover analysis is executed up to  $\theta_r$  of 10%. Pushover

curves are shown along with structural limit states and  $\theta_r$  estimations under the FOE, DBE and MCE.

Fig. 7(a) shows the pushover curve of CP3D100W. WHPs yield at  $\theta_r$  lower than the FOE  $\theta_r$  (0.58%) followed by column plastic hinge and fuse activation at the DBE  $\theta_r$  (1.59%). Plastic hinge at the end of the beam flange reinforcing plate occurs at the MCE  $\theta_r$  (2.44%). After this point the strength of CP3D100W continues to increase up to  $\theta_r$  of 5.5% where beam local buckling occurs and strength deterioration initiates. The behaviour of CP3D100W is consistent with the target performance of minor beam yielding ( $\varepsilon/\varepsilon_y=2$ ) and fuse activation under the DBE. PT bars do not yield even under very large drifts as the beam plastic hinge rotations drastically reduce gap opening and PT bar elongation. The peak  $V/W$  is 0.32. Viscous dampers do not affect the behaviour of the SC-MRFs under static loading, and so, HP20D100W has the same pushover curve (Fig. 7(b)) with CP3D100W apart from lower  $\theta_r$  under the FOE, DBE and MCE. The behaviour of HP20D100W is consistent with the target performance of  $\varepsilon/\varepsilon_y=1$  under the DBE and fuse activation under the MCE. Column plastic hinge occurs at the MCE  $\theta_r$  (1.6%), while beam plastic hinge occurs at  $\theta_r$  higher than the MCE  $\theta_r$ .

Fig. 7(c) shows the pushover curve of CP11D86W. WHPs yield at  $\theta_r$  lower than the FOE  $\theta_r$  (0.59%) followed by fuse activation close to the DBE  $\theta_r$  (1.52%). Column and beam plastic hinge occurs at the MCE  $\theta_r$  (2.40%). The beam plastic hinge rotation capacity is reached at 6%  $\theta_r$ . The behaviour of CP11D86W is consistent with the target performance of minor beam yielding ( $\varepsilon/\varepsilon_y=2$ ) and fuse activation under the DBE. The peak  $V/W$  is 0.16. HP19.5D86W has the same pushover curve (Fig. 7(d)) with CP11D86W apart from lower  $\theta_r$  under the FOE, DBE and MCE. The behaviour of CP11D86W is consistent with the target performance of  $\varepsilon/\varepsilon_y=1.3$  under the DBE and fuse activation under a seismic intensity of 1.2 times the DBE. Column plastic hinge and beam plastic hinge occur at  $\theta_r$  higher than the MCE  $\theta_r$  (1.95%).

Fig. 7(e) shows the pushover curve of CP22D70W. WHPs yield at  $\theta_r$  lower than the FOE  $\theta_r$  (0.61%) followed by fuse activation and beam plastic hinge after the DBE  $\theta_r$  (1.50%). The descending branch of the pushover curve initiates at the MCE  $\theta_r$  (2.23%) solely due to excessive P- $\Delta$  effects. Column plastic hinge occurs at 7.1%  $\theta_r$  followed by beam local buckling at 8.2%  $\theta_r$ . The behaviour of CP22D70W is consistent with the target performance of minor beam yielding ( $\varepsilon/\varepsilon_y=2$ ) and fuse activation under the DBE. The peak  $V/W$  is 0.11.

Fig. 7(f) shows the pushover curve of the conventional MRF. Column plastic hinge occurs at 0.55%  $\theta_r$  followed by beam plastic hinge formation at 1.03%  $\theta_r$  and beam local buckling at 3.0%  $\theta_r$ . The behaviour of the conventional MRF is worse than the behaviour of the CP3D100W SC-MRF with the same cross-sections as all structural limit states are reached at lower  $\theta_r$ . The peak  $V/W$  is 0.26.

Fig. 8 shows the  $V/W$ - $\theta_r$  behaviour of the SC-MRFs and the conventional MRF from nonlinear cyclic (push-pull) static analysis up to the DBE  $\theta_r$ . All SC-MRFs have good energy dissipation capacity and self-centering capability. CP3D100W has a small residual  $\theta_r$  due to modest column base yielding. The conventional MRF shows higher energy dissipation capacity but has significant residual  $\theta_r$  compared to all SC-MRFs.

Fig. 9 shows the pushover curve of CP3D100W with and without the fuse devices. The behaviour of both systems is exactly the same up to DBE, since the fuse devices were designed to be activated under the DBE. For both cases there is no PT bar yielding. However, the CP3D100W with fuse devices experiences beam local buckling at higher  $\theta_r$ , which demonstrates the effectiveness of the fuse devices to improve the structural seismic performance of steel SC-MRFs.

## 7. Fragilities under the DBE and MCE

### 7.1 Ground motions

A set of 22 recorded far-field ground motion pairs (i.e. 44 time histories) developed by the ATC-63 project [6] are used for nonlinear time history analyses. Ground motions were recorded on stiff soil, do not exhibit pulse-type near-fault characteristics, and were scaled at the DBE and MCE where seismic intensity is represented by the 5% spectral acceleration,  $S_a$ , at  $T$  from the OpenSees models in Section 5.

### 7.2 Nonlinear dynamic analysis

The Newmark method with constant acceleration is used to integrate the equations of motion. The Newton method with tangent stiffness is used to minimize the unbalanced forces within each integration time step. A Rayleigh damping matrix is used to model the inherent 3% critical damping at the first two modes of vibration. A nonlinear force-controlled static analysis under gravity loads and the applied post-tensioning is first performed. The stiff truss elements that simulate diaphragm action are not included in the SC-MRF model for this analysis to allow post tensioning and initial beam shortening without the slab presence. Then, the stiff truss elements are added into the model and the nonlinear dynamic analysis is executed. Each dynamic analysis is extended well beyond the actual earthquake time to allow for damped free vibration decay and accurate  $\theta_{s,res}$  calculation.

### 7.3 Fragilities

Having  $\theta_{s,max}$  and  $\theta_{s,res}$  for a SC-MRF from nonlinear dynamic analyses using the 44 ground motions of Section 7.1 scaled at a specific seismic intensity, a fragility curve is constructed by fitting a lognormal cumulative distribution function to the ranked probabilities of non-exceedance, as shown in Fig. 10(a) for the CP3D100W under the DBE.

Fig. 10(b) shows the  $\theta_{s,max}$  fragility curves of the SC-MRFs and the conventional MRF under the DBE. The  $\theta_{s,max}$  at 50% probability of non-exceedance is 1.54% for the CP3D100W, 1.01% for the HP20D100W, 1.44% for the CP11D86W, 1.07% for the HP19.5D86W, 1.47% for the CP22D70W and 1.74% for the conventional MRF. These values are smaller than the design DBE  $\theta_{s,max}$  values in Table 1 because the centerline models used for design are more flexible than the OpenSees models used in seismic analyses (see last paragraph of Section 5). HP20D100W and HP19.5D86W have significantly better performance with fragility curves clearly shifted to the left of those of the other SC-MRFs. This demonstrates the effectiveness of supplemental damping to improve the structural and non-structural seismic performance of steel SC-MRFs. Although designed for different  $\theta_{s,max}$  (1.2% vs. 1.5%), HP20D100W and HP19.5D86W have almost identical performance with no evident differences among their fragility curves. The other SC-MRFs, CP3D100W, CP11D86W CP22D70W (all designed for 1.8%  $\theta_{s,max}$ ) have almost identical performance apart from probabilities of non-exceedance higher than 70% for which CP22D70W has a worse performance. This demonstrates that steel SC-MRFs with viscous dampers can be designed for less steel weight without compromising their DBE performance. For probabilities of non-exceedance lower than 70%, the conventional MRF has worse performance compared to the SC-MRFs.

Fig. 10(c) shows the  $\theta_{s,max}$  fragility curves of the SC-MRFs and the conventional MRF under the MCE. The  $\theta_{s,max}$  at 50% probability of non-exceedance is 2.32% for the CP3D100W, 1.54% for the HP20D100W, 2.36% for the CP11D86W, 1.85% for the HP19.5D86W, 2.56% for the CP22D70W and 2.3% for the conventional MRF. These values are lower than the design MCE  $\theta_{s,max}$  values in Table 1 for the reason explained in the

previous paragraph. Similar to the DBE case, HP20D100W and HP19.5D86W have significantly better performance with fragility curves shifted to the left with respect to those of the other SC-MRFs. Contrary to the DBE case, HP20D100W has clearly better MCE performance than that of HP19.5D86W. CP3D100W, CP11D86W and the MRF have almost identical performance. Contrary to the DBE case, CP22D70W has worse MCE performance than that of CP3D100W and CP11D86W. These results demonstrate that steel SC-MRFs with viscous dampers can be generally designed for less steel weight without compromising their MCE performance; yet a restriction on the strength reduction may need to be established.

Fig. 11(a) shows the  $\theta_{s,res}$  fragility curves of the SC-MRFs and the conventional MRF under the DBE. CP3D100W (that experiences larger plastic deformations at the column bases compared to the other SC-MRFs; see Section 6) has the largest  $\theta_{s,res}$  among the SC-MRFs with a value of 0.1% at 50% probability of non-exceedance. This  $\theta_{s,res}$  value is lower than the global sway imperfections defined in EC3, and so, is considered very small. HP20D100W eliminates  $\theta_{s,res}$ . This demonstrates the effectiveness of supplemental damping to improve the  $\theta_{s,res}$  performance of SC-MRFs. In general, Fig. 11(a) shows that the proposed design procedure results in SC-MRFs that eliminate  $\theta_{s,res}$  under the DBE, whereas the conventional MRF has high  $\theta_{s,res}$  with a value of 0.49% at 50% probability of non-exceedance.

Fig. 11(b) shows the  $\theta_{s,res}$  fragility curves of the SC-MRFs and the conventional MRF under the MCE. CP3D100W has the largest  $\theta_{s,res}$  among the SC-MRFs with a value of 0.17% at 50% probability of non-exceedance. This  $\theta_{s,res}$  value is lower than the global sway imperfections defined in EC3 [31], and so, is considered very small. All the other SC-MRFs have  $\theta_{s,res}$  lower or equal than 0.1% at 50% probability of non-exceedance. Similar to the DBE case, Fig. 11(b) shows the effectiveness of supplemental damping to improve the  $\theta_{s,res}$  performance and that the proposed design procedure results in SC-MRFs with very low  $\theta_{s,res}$  under the MCE. The conventional MRF has significant  $\theta_{s,res}$  with a value of 0.75% at 50% probability of non-exceedance. It should be noted that a building may have to be demolished if the  $\theta_{s,res}$  is higher than 0.5% [38].

## 8. Collapse resistance

None of the SC-MRFs and the conventional MRF becomes globally unstable under the MCE ground motions. This shows that SC-MRFs having different strength, stiffness and supplemental damping but designed according to the proposed design procedure that enforces the minimum EC8 strength ( $q=6.5$  with respect to the highly damped spectrum) and drift ( $\theta_{s,max}=0.75\%$  under the FOE) requirements, eliminate the probability of collapse under the MCE.

The collapse seismic intensity under a specific ground motion can be identified using incremental dynamic analysis (IDA) [39], i.e. scaling up in small increments the ground motion intensity until the SC-MRF becomes unstable [6]. Iterations and smaller increments are needed to identify the maximum possible seismic intensity for which the SC-MRF is stable. This approach is extremely time consuming for the computationally demanding SC-MRFs models that incorporate difficult to converge contact elements in the PT connections. This work investigates the collapse resistance of the SC-MRFs and the conventional MRF solely for seismic intensities equal or lower than two times the MCE (2MCE).

The ground motions were scaled at the 2MCE and dynamic analyses were conducted. The ground motions producing stable response are considered as non-collapse cases. For the rest ground motions (resulting in non-convergence or convergence at unrealistic  $\theta_{s,max}$  larger than 10%), IDA is employed to ensure that they genuinely represent collapse cases for seismic intensities equal or lower than the 2MCE. Fig. 12 shows the IDA curves associated with the collapse cases where the seismic intensity is represented by  $S_a$  normalized by  $S_{a,MCE}$ , i.e. the

MCE spectral acceleration of the ground motion at  $T$ . The 2MCE probabilities of collapse (simply calculated as the ratio of the collapse cases to the number of ground motions) are 4.5% for CP3D100W, 2.2% for HP20D100W, 9.1% for CP11D86W, 6.8% for HP19.5D86W, 9.1% for CP22D70W, and 20.5% for the conventional MRF. These results highlight the superior collapse resistance of SC-MRFs with fuse-PT bars and viscous dampers compared to conventional MRFs even when the SC-MRF is significantly lighter than the conventional MRF. These results also highlight that providing supplemental damping along with enforcing stricter design criteria for the PT connections can significantly improve the collapse resistance of SC-MRFs, e.g. the 2MCE probability of collapse of CP3D100W and HP20D100W (SC-MRFs with the same cross-sections) are 4.5% and 2.2%, respectively.

## 9. Conclusions

This paper focused on the seismic design and assessment of steel SC-MRFs with viscous dampers within the framework of EC8. The procedure used to design the SC-MRFs defines performance levels with respect to drifts, residual drifts, plastic deformations in column bases and limit states in the PT connections. A preliminary pushover analysis is conducted at the early phase of the design procedure to estimate rotations and axial forces in PT connections. A prototype building was designed as an SC-MRF with or without viscous dampers. SC-MRF designs with different base shear strength and supplemental damping were investigated. Pushover and seismic analyses were conducted in OpenSees using models capable to capture all structural limit states up to collapse. Based on the results presented in the paper, the following conclusions are drawn:

1. The preliminary pushover analysis makes the design procedure very accurate in predicting structural limit states. The use of the fuse-PT bar system and the  $\gamma_{PT}$  factor delay beam local buckling and eliminate the possibility of PT bar yielding.
2. The SC-MRFs designed in this paper avoid beam and column base plastic hinge formation under the MCE and experience strength deterioration at roof drifts higher than 5%.
3. Strict design criteria for the PT connections along with a low peak storey drift target value should be enforced to genuinely achieve seismic resilience, e.g. rapid return to building occupancy after the DBE.
4. SC-MRFs with viscous dampers can be designed for less steel weight (resulting in less strength) without compromising their DBE drift performance. The same is generally true for the MCE drift performance; yet a restriction on the strength reduction should be established.
5. Supplemental damping is very effective in improving the residual drift performance of SC-MRFs.
6. SC-MRFs with different strength, stiffness and supplemental damping but designed according to the proposed design procedure that enforces the minimum EC8 strength ( $q=6.5$  with respect to the highly damped spectrum) and drift ( $\theta_{s,max}=0.75\%$  under the FOE) requirements, eliminate the probability of collapse under the MCE.
7. Supplemental damping along with strict design criteria for the PT connections can significantly improve the collapse resistance of SC-MRFs.
8. SC-MRFs with fuse-PT bars and viscous dampers have superior collapse resistance compared to conventional steel MRFs even when the SC-MRF is significantly lighter than the conventional MRF.

## Acknowledgements



Financial support for this work is provided by the Engineering and Physical Sciences Research Council of the United Kingdom; Grant Ref: EP/K006118/1.

*This paper is dedicated to the memory of Professor Nikitas Bazeos (Department of Civil Engineering, University of Patras, Greece); a great teacher, advisor and friend.*

## References

- [1] Sanchez-Ricart L, Plumier A. Parametric study of ductile moment-resisting steel frames: A first step towards Eurocode 8 calibration. *Earthquake Engineering and Structural Dynamics* 2008; 37(7): 1135–1155.
- [2] Elghazouli AY. Assessment of European seismic design procedures for steel framed structures. *Bulletin of Earthquake Engineering* 2010; 8:65–89.
- [3] Tzimas AS, Karavasilis TL, Bazeos N, Beskos DE. A hybrid force/displacement seismic design method for steel building frames. *Engineering Structures* 2013; 56: 1452-1463.
- [4] EC8. Eurocode 8. Design of structures for earthquake resistance; 2013.
- [5] Dolce M, Manfredi G. Research needs in earthquake engineering highlighted by the 2009 L'Aquila earthquake. The ReLUIS-DPC Project Report; 2009.
- [6] FEMA P695. Quantification of building seismic performance factors. ATC-63 Project. Applied Technology Council. CA. USA; 2008.
- [7] Ricles J, Sause R, Garlock M, Zhao C. Posttensioned seismic-resistant connections for steel frames. *Journal of Structural Engineering* 2001; 127(2): 113-121.
- [8] Christopoulos C, Filiatrault A, Uang CM, Folz B. Posttensioned energy dissipating connections for moment-resisting steel frames. *Journal of Structural Engineering (ASCE)* 2002; 128(9): 1111-1120.
- [9] Chou CC, Lai YJ. Post-tensioned self-centering moment connections with beam bottom flange energy dissipators. *Journal of Constructional Steel Research* 2009; 65(10-11): 1931-1941.
- [10] Chou C-C, Tsai K-C, Yang W-C. Self-centering steel connections with steel bars and a discontinuous composite slab. *Earthquake Engineering and Structural Dynamics* 2009; 38: 403-422.
- [11] Vasdravellis G, Karavasilis TL, Uy B. Large-scale experimental validation of steel post-tensioned connections with web hourglass pins. *Journal of Structural Engineering* 2013; 139(6):1033-1042.
- [12] Vasdravellis G, Karavasilis TL, Uy B. Finite element models and cyclic behaviour of self-centering post-tensioned connections with web hourglass pins. *Engineering Structures* 2013; 52:1-16.
- [13] Dimopoulos A, Karavasilis TL, Vasdravellis G, Uy B. Seismic design, modelling and assessment of self-centering steel frames using post-tensioned connections with web hourglass shape pins. *Bulletin of Earthquake Engineering* 2013; 11:1797–1816.
- [14] Rojas P, Ricles JM, Sause R. Seismic performance of post-tensioned steel moment resisting frames with friction devices. *Journal of Structural Engineering* 2004; 131(4): 529-540.
- [15] Kim HJ, Christopoulos C. Friction damped posttensioned self-centering steel moment-resisting frames. *Journal of Structural Engineering* 2008; 134(11): 1768-1779.
- [16] Tsai KC, Chou CC, Lin CL, Chen PC, Jhang SJ. Seismic self-centering steel beam-to-column moment connections using bolted friction devices. *Earthquake Engineering and Structural Dynamics* 2008; 37: 627-645.

- [17] Wolski M, Ricles JM, Sause R. Experimental study of a self-centering beam-column connection with bottom flange friction device. *Journal of Structural Engineering* 2009; 135(5): 479-488.
- [18] Garlock M, Sause R, Ricles JM. Behavior and design of posttensioned steel frame systems. *Journal of Structural Engineering* 2007; 133(3): 389-399.
- [19] Kim HJ, Christopoulos C. Seismic design procedure and seismic response of post-tensioned self-centering steel frames. *Earthquake Engineering and Structural Dynamics* 2008; 38(3): 355-376.
- [20] Karavasilis TL, Sause R, Ricles JM. Seismic design and evaluation of steel MRFs with compressed elastomer dampers. *Earthquake Engineering and Structural Dynamics* 2012; 41(3): 411-429.
- [21] Karavasilis TL, Ricles JM, Sause R, Chen C. Experimental evaluation of the seismic performance of steel MRFs with compressed elastomer dampers using large-scale real-time hybrid simulation. *Engineering Structures* 2011; 33(6):1859-1869.
- [22] Karavasilis TL, Kerawala S, Hale E. Model for hysteretic behaviour of steel energy dissipation devices and evaluation of a minimal-damage seismic design approach for steel frames. *Journal of Constructional Steel Research* 2012; 70:358-367.
- [23] Karavasilis TL, Seo C-Y. Seismic structural and non-structural performance evaluation of highly damped self-centering and conventional systems. *Engineering Structures* 2011; 33: 2248-2258.
- [24] Seo C-Y, Karavasilis TL, Ricles JM, Sause R. Seismic performance and probabilistic collapse resistance assessment of steel moment resisting frames with fluid viscous dampers. *Earthquake Engineering and Structural Dynamics*. In press.
- [25] Kurama YC. Seismic design of unbonded post-tensioned precast concrete walls with supplementary viscous damping. *ACI Structural Journal* 2000; 97(3):648-658.
- [26] Kam WY, Pampanin S, Palermo A, Carr AJ. Self-centering structural systems with combination of hysteretic and viscous energy dissipations. *Earthquake Engineering and Structural Dynamics* 2010; 39(10): 1083-1108.
- [27] Kam WY, Pampanin S, Carr AJ, Palermo A. Design procedure and behaviour of advanced flag-shape (AFS) MDOF systems. *NZSEE Conference*; 2008.
- [28] Mazzoni S, McKenna F, Scott M, Fenves G. Open system for earthquake engineering simulation (OpenSees). *User Command Language Manual*, Pacific Earthquake Engineering Research Center, University of California, Berkeley; 2006.
- [29] Vasdravellis G, Karavasilis TL, Uy B. Design rules, experimental evaluation, and fracture models for high-strength and stainless steel hourglass shape energy dissipation devices. *Journal of Structural Engineering* 2014; under review.
- [30] Lin YC, Sause R, Ricles JM. Seismic performance of a large-scale steel self-centering moment resisting frame: MCE hybrid simulations and quasi-static pushover tests. *Journal of Structural Engineering* 2013; 139(7): 1227-1236.
- [31] EC3. Eurocode 3: design of steel structures- Part 1-1: general rules and rules for steel buildings; 2010.
- [32] Whittaker AS, Constantinou MC, Ramirez OM, Johnson MW, Chrysostomou CZ. Equivalent lateral force and modal analysis procedures of the 2000 NEHRP Provisions for buildings with damping systems. *Earthquake Spectra* 2003; 19(4):959-80.
- [33] Whittle J, Williams MS, Karavasilis TL, Blakeborough A. A comparison of viscous damper placement methods for improving seismic building design. *Journal of Earthquake Engineering* 2012; 16: 540-560.
- [34] Federal Emergency Management Agency, FEMA. NEHRP guidelines for the seismic rehabilitation of buildings. Report FEMA-273. Washington (DC); 1997.

- [35] Newell J, Uang C-M. Cyclic behaviour of steel columns with combined high axial load and drift demand. Report No. SSRP-06/22. Department of Structural Engineering, University of California, San Diego, La Jolla. 2006.
- [36] Lignos DG, Krawinkler H. A database in support of modeling of component deterioration for collapse prediction of steel frame structures. ASCE Structures Congress, SEI institute, Long Beach CA; 2007.
- [37] Charney FA, Downs WM. Connections in steel structures V. ESSC/AISC Workshop. Amsterdam, June 3-4; 2004.
- [38] McCormick J, Aburano H, Ikenaga M, Nakashima M. Permissible residual deformation levels for building structures considering both safety and human elements. 14<sup>th</sup> World Conference of Earthquake Engineering, Beijing, China; 2008.
- [39] Vamvatsikos D, Cornell CA. Incremental dynamic analysis. *Earthquake Engineering and Structural Dynamics* 2002; 31(3): 491-514.

**Table 1**

Data and design criteria for the SC-MRFs with viscous dampers

SC-MRF	Steel weight <sup>a</sup> (kN)	$T$ (s.)	$\zeta_t$ (%)	$\theta_{s,max}$ FOE (%)	$\theta_{s,max}$ DBE (%)	$\theta_{s,max}$ MCE (%)	$\varepsilon_c/\varepsilon_y$ (DBE)	$\gamma_{PT}$	$\theta_4$ fuse activation
CP3D100W	268	1.27	3.00	0.72	1.80	2.70	2.0	2.1	$\theta_{DBE}^b$
HP20D100W	268	1.27	20.0	0.48	1.20	1.80	1.0	3.5	$1.5\theta_{DBE}$
CP11D86W	230	1.63	11.0	0.72	1.80	2.70	2.0	2.1	$\theta_{DBE}$
HP19.5D86W	230	1.63	19.5	0.60	1.50	2.25	1.3	2.6	$1.2\theta_{DBE}$
CP22D70W	190	2.22	22.0	0.72	1.80	2.70	2.0	2.1	$\theta_{DBE}$

<sup>a</sup> Beams and columns; <sup>b</sup> see Table 2

**Table 2** $\theta_{DBE}$  and  $\theta_{MCE}$  (in rads) used to design the PT connections of the SC-MRFs

Storey	CP3D100W		HP20D100W		CP11D86W		HP19.5D86W		CP22D70W	
	$\theta_{DBE}$	$\theta_{MCE}$	$\theta_{DBE}$	$\theta_{MCE}$	$\theta_{DBE}$	$\theta_{MCE}$	$\theta_{DBE}$	$\theta_{MCE}$	$\theta_{DBE}$	$\theta_{MCE}$
1	0.013	0.0227	0.0078	0.013	0.0113	0.0197	0.0094	0.015	0.0123	0.0183
2	0.015	0.0243	0.009	0.015	0.0143	0.0231	0.0116	0.0185	0.0146	0.0222
3	0.015	0.0238	0.0088	0.015	0.0156	0.0245	0.0126	0.02	0.0166	0.0249
4	0.0127	0.0209	0.0068	0.0127	0.0151	0.0236	0.012	0.0194	0.017	0.0253
5	0.0101	0.0179	0.0042	0.0101	0.0133	0.0216	0.0103	0.0175	0.015	0.0234

**Table 3**  
Design details for the CP3D100W and HP20D100W SC-MRFs

Storey	Cross sections			PT bars		WHPs			Reinforcing plates			Fuse	Viscous dampers c (kN·(s./m) <sup>0.5</sup> )	
	Beams	Columns	Gravity columns	$T_0$ (kN)	$d_{PT}$ (mm)	$D_e$ (mm)	$D_i$ (mm)	$L_{WHP}$ (mm)	$L_{rp}$ (mm)	$A_{rp}$ (mm <sup>2</sup> )	$A_{fuse}$ (mm <sup>2</sup> )	CP3D100W	HP20D100W	
1	IPE550	HEB650	HEB240	1087	43	43	33	70	1258	6720	6870	-	1156	
2	IPE600	HEB650	HEB240	1256	50	46	36	70	1461	8580	9150	-	887	
3	IPE550	HEB650	HEB240	1087	43	44	33	70	1311	6720	7210	-	765	
4	IPE500	HEB600	HEB220	941	37	41	30	70	1073	5200	5490	-	596	
5	IPE500	HEB600	HEB220	941	35	39	28	70	724	4200	5060	-	438	

**Table 4**

Design details for the CP11D86W and HP19.5D86W SC-MRFs

Storey	Cross sections			PT bars			WHPs		Reinforcing plates			Fuse	Dampers $c$ (kN·(s./m) <sup>0.5</sup> )	
	Beams	Columns	Gravity columns	$T_0$ (kN)	$d_{PT}$ (mm)	$D_e$ (mm)	$D_i$ (mm)	$L_{WHP}$ (mm)	$L_{rp}$ (mm)	$A_{rp}$ (mm <sup>2</sup> )	$A_{fuse}$ (mm <sup>2</sup> )	CP11D86W	HP19.5D86W	
1	IPE450	HEB600	HEB240	811	33	40	29	70	942	3990	4400	961	1812	
2	IPE500	HEB600	HEB240	941	39	42	32	70	1150	5200	5850	676	1275	
3	IPE450	HEB600	HEB240	811	35	40	29	70	1129	4370	4920	549	1035	
4	IPE400	HEB550	HEB220	701	30	38	27	70	1065	3600	3910	426	803	
5	IPE400	HEB550	HEB220	701	30	36	25	70	829	3240	3800	279	525	

**Table 5**  
Design details for the CP22D70W SC-MRF

Storey	Cross sections		PT bars		WHPs			Reinforcing plates			Fuse	Dampers $c$ (kN·(s/m) <sup>0.5</sup> )
	Beams	Columns	Gravity columns	$T_0$ (kN)	$d_{PT}$ (mm)	$D_e$ (mm)	$D_i$ (mm)	$L_{WHP}$ (mm)	$L_{rp}$ (mm)	$A_{rp}$ (mm <sup>2</sup> )	$A_{fuse}$ (mm <sup>2</sup> )	CP22D70W
1	IPE360	HEB500	HEB240	607	27	36	25	70	867	2890	3135	1655
2	IPE400	HEB500	HEB240	701	30	39	28	70	961	3420	3880	1094
3	IPE360	HEB500	HEB240	607	28	37	25	70	953	2890	3382	877
4	IPE330	HEB450	HEB220	523	25	35	24	70	992	2560	2822	666
5	IPE330	HEB450	HEB220	523	25	33	22	70	745	2240	2753	435



## CAPTIONS FOR FIGURES

**Fig. 1.** (a) SC-MRF; (b) exterior PT connection with WHPs; and (c) WHP geometry and assumed static system

**Fig. 2.** Discontinuous steel-concrete composite slab details

**Fig. 3.** (a) Free body diagram of an external PT connection; and (b) SC-MRF expansion and horizontal forces equilibrium

**Fig. 4.** (a) Theoretical cyclic behaviour of the PT connection with WHPs; (b) moment contribution from  $N$ ; and (c) moment contribution from the WHPs

**Fig. 5.** (a) Plan and (b) elevation of the prototype building

**Fig. 6.** Model for an exterior PT connection and the associated beams and columns

**Fig. 7.** Base shear coefficient - roof drift behaviour from nonlinear monotonic (pushover) static analysis.

**Fig. 8.** Base shear coefficient - roof drift behaviour from nonlinear cyclic (push-pull) static analysis up to DBE roof drift

**Fig. 9.** Base shear coefficient - roof drift behaviour from nonlinear monotonic (pushover) static analysis of CP3D100W with and without fuse elements

**Fig. 10.** (a): Fitted  $\theta_{s,max}$  lognormal cumulative distribution function for the CP3D100W under the DBE; (b)  $\theta_{s,max}$  fragility curves under the DBE; (c)  $\theta_{s,max}$  fragility curves under the MCE

**Fig. 11.**  $\theta_{s,res}$  fragility curves: (a) DBE and (b) MCE

**Fig. 12.** IDA curves associated with collapse at seismic intensities lower than 2MCE

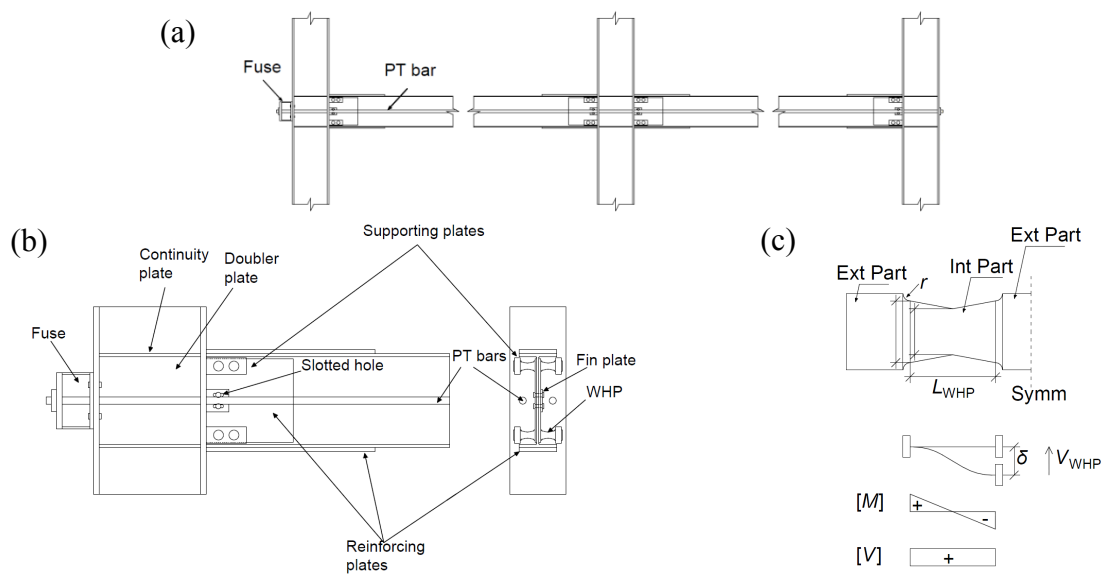


**Fig. 1**

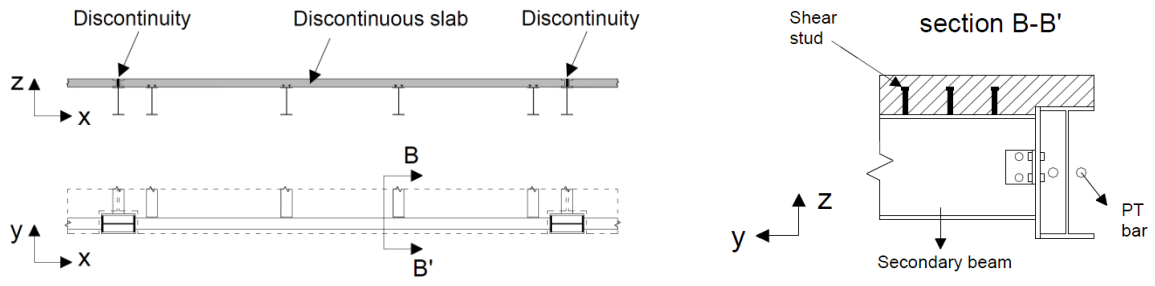


**Fig. 2**

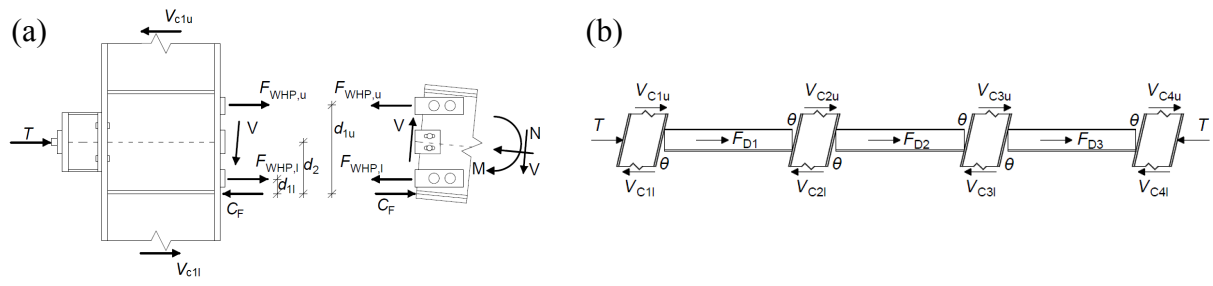


**Fig. 3**

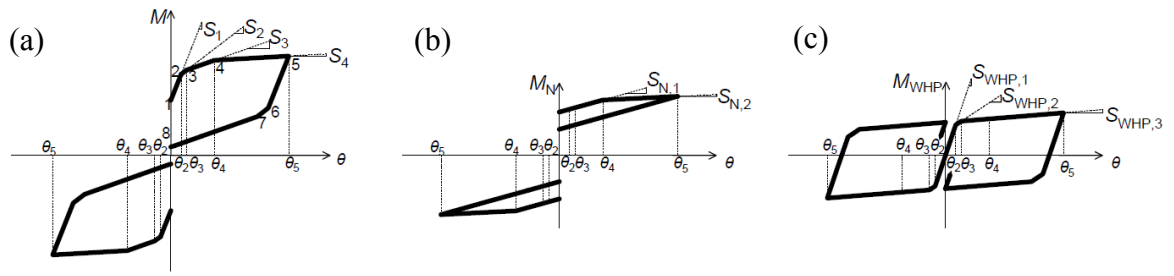


**Fig. 4**

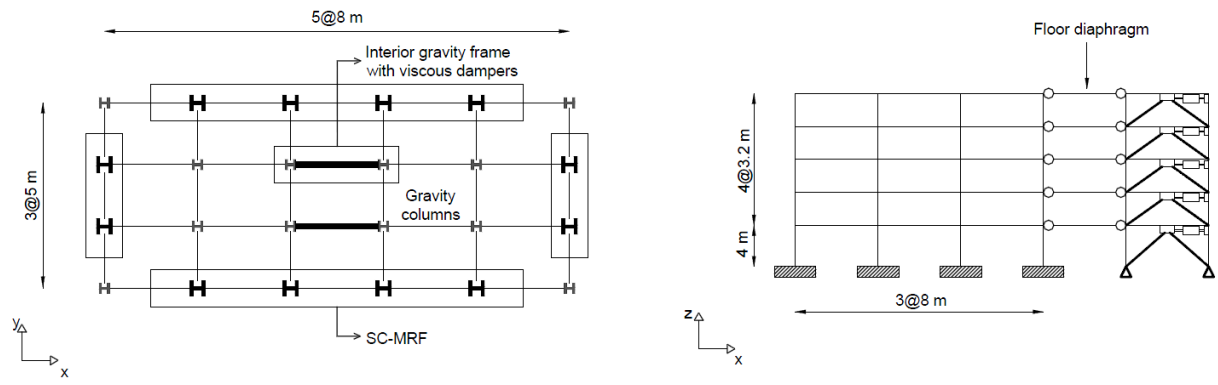


**Fig. 5**

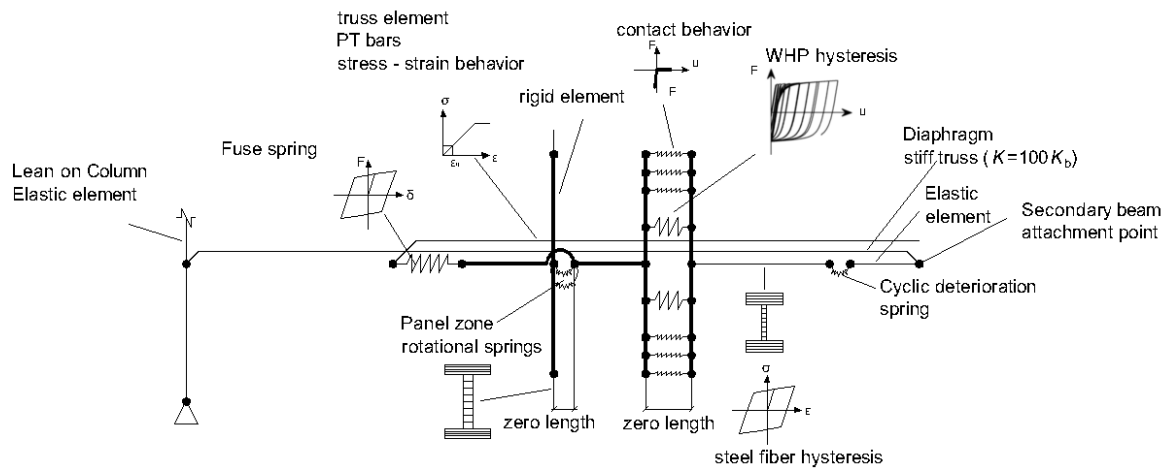


**Fig. 6**

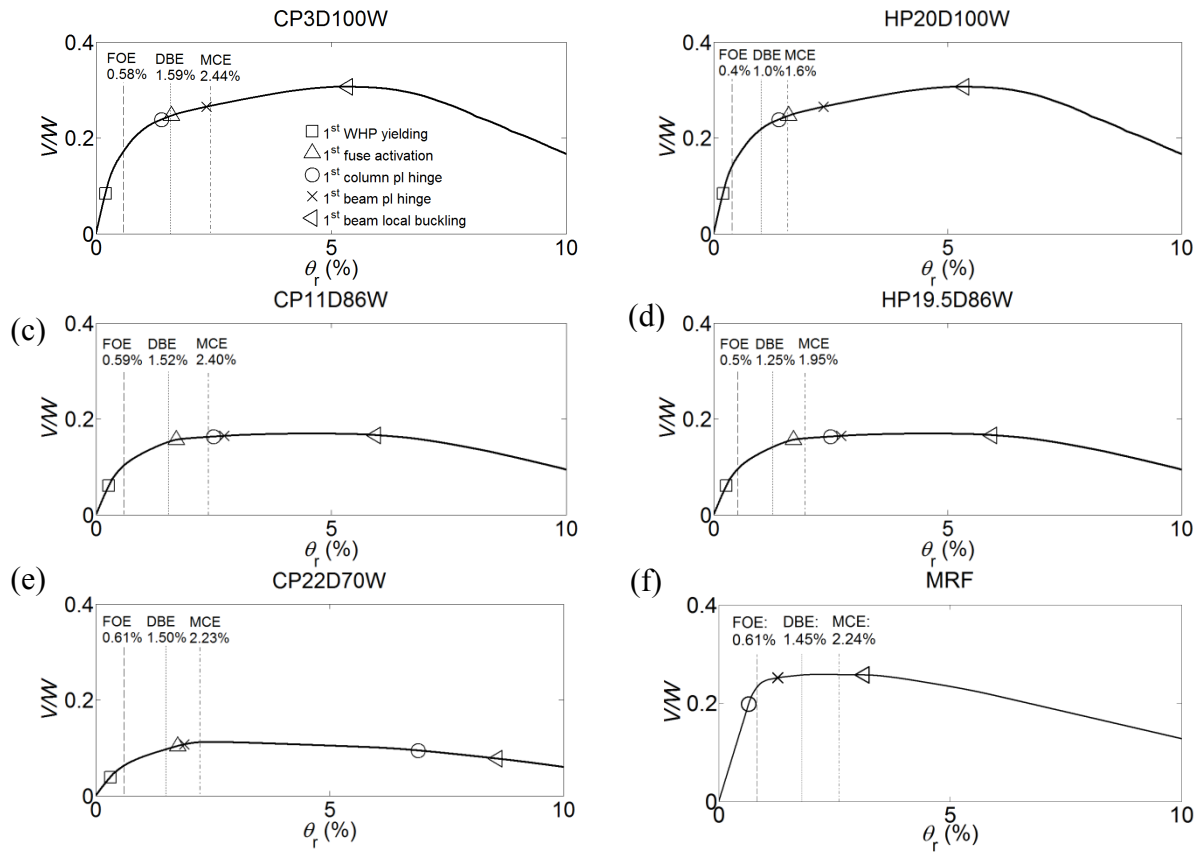
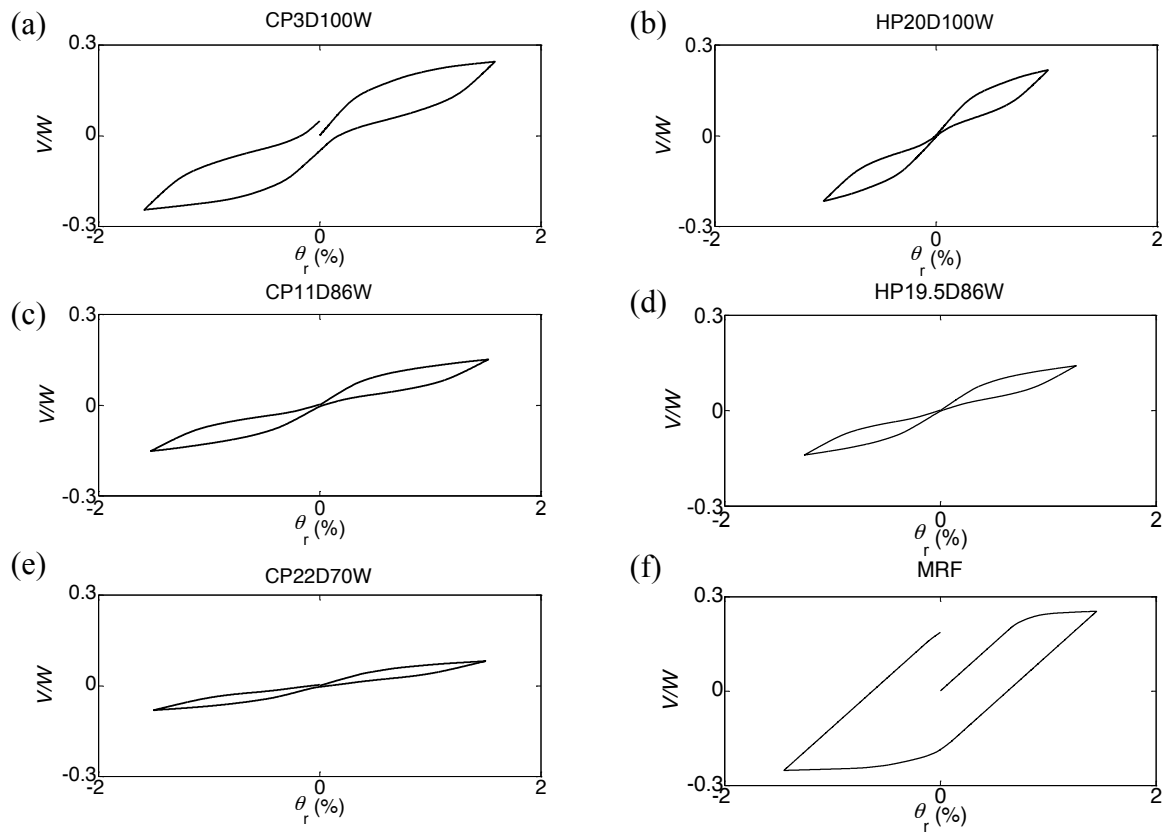
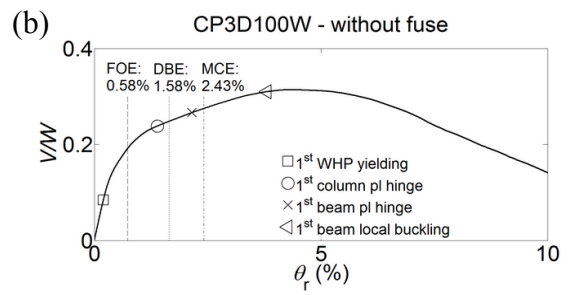
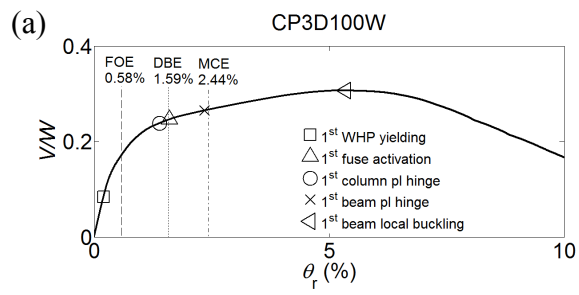


Fig. 7





**Fig. 8**



**Fig. 9**

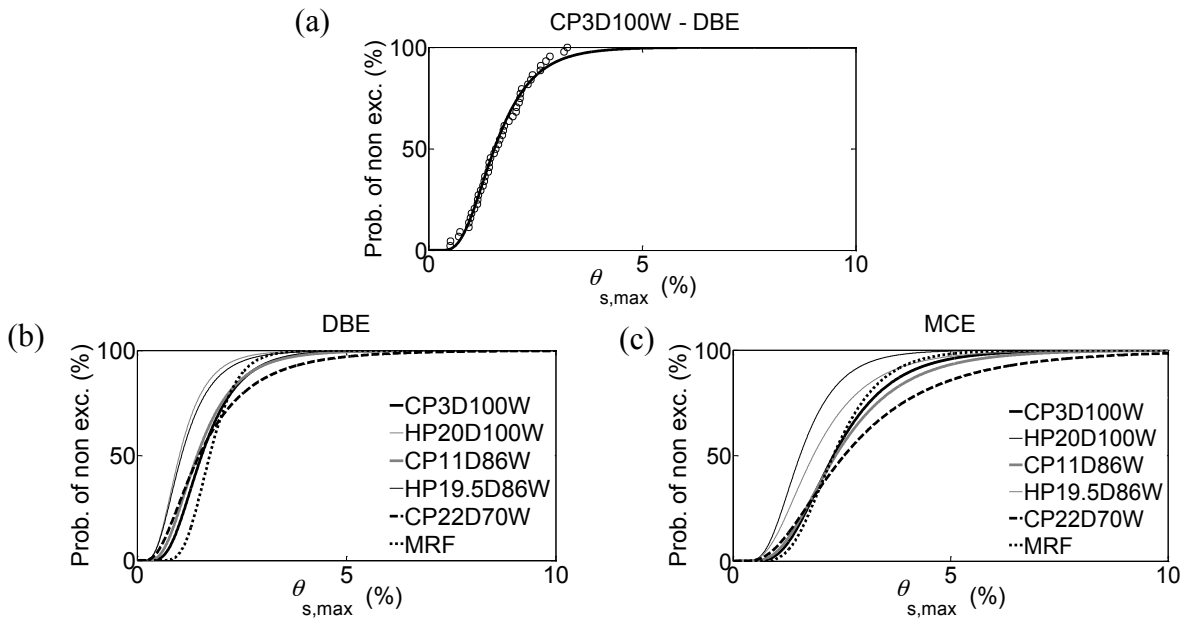


**Fig. 10**

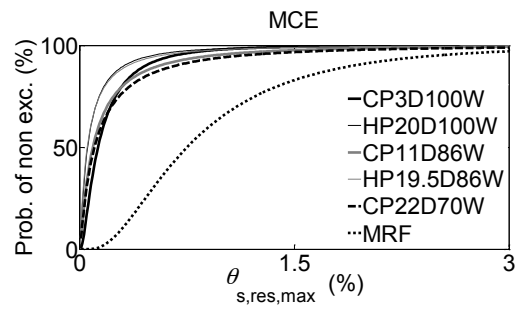
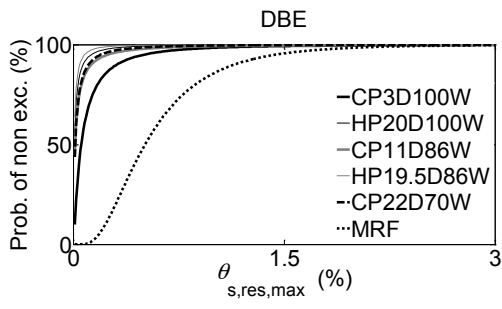


**Fig. 11**

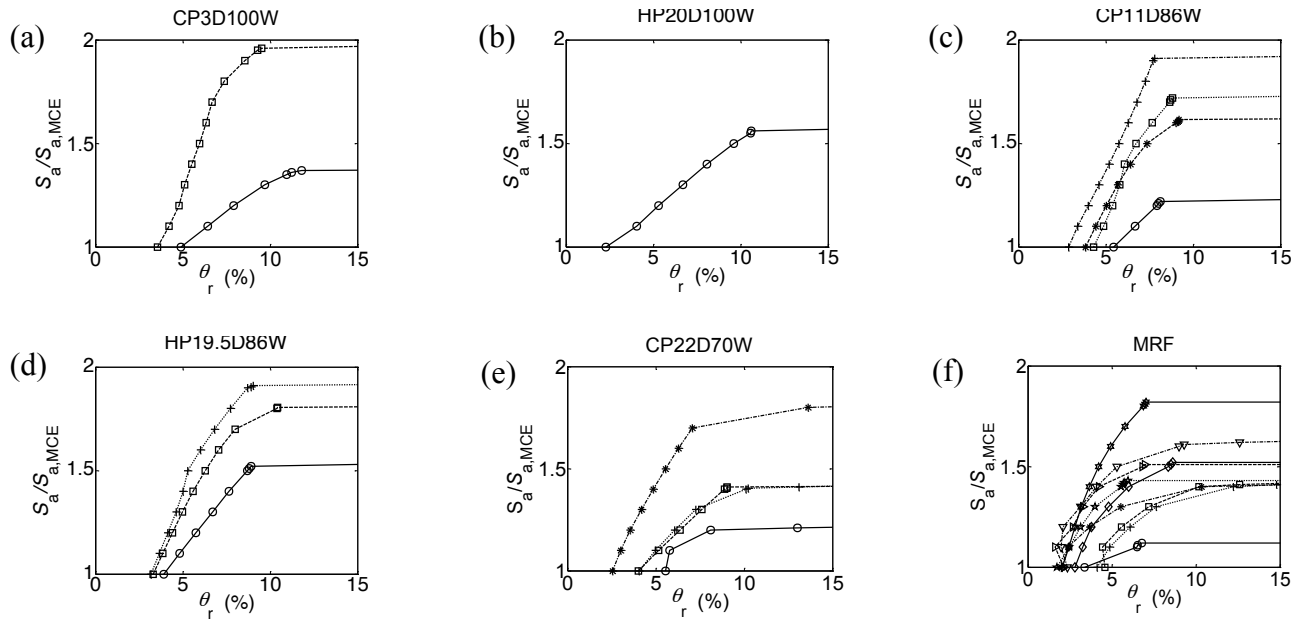


**Fig. 12**